J|A|C|S ARTICLES

Published on Web 06/04/2010

# On the Origin of Increased Phonon Scattering in Nanostructured PbTe Based Thermoelectric Materials

Jiaqing He,*[,†,‡] Joseph R. Sootsman,[‡] Steven N. Girard,[‡] Jin-Cheng Zheng,[§] Jianguo Wen,[||] Yimei Zhu,[⊥] Mercouri G. Kanatzidis,*[,‡,#] and Vinayak P. Dravid*[,†]

*Department of Materials Science and Engineering, Northwestern University, Evanston, Illinois 60208, Department of Chemistry, Northwestern University, Evanston, Illinois 60208, Department of Physics, and Institute of Theoretical Physics and Astrophysics and Fujian Key Lab of Semiconductor Materials and Applications, Xiamen University, Xiamen 361005, P. R. China, Center for Microanalysis of Materials, Frederick Seitz Materials Research Laboratory, University of Illinois at Urbana−Champaign, Urbana, Illinois 61801, Department of Condensed Matter and Materials Science, Brookhaven National Laboratory, Upton, New York 11973, and Materials Science Division, Argonne National Laboratory, Argonne, Illinois 60439*

Received February 12, 2010; E-mail: jiaqing-he@northwestern.edu; v-dravid@northwestern.edu; m-kanatzidis@northwestern.edu

***Abstract:*** We have investigated the possible mechanisms of phonon scattering by nanostructures and defects in PbTe-X (X = 2% Sb, Bi, or Pb) thermoelectric materials systems. We find that among these three compositions, PbTe-2% Sb has the lowest lattice thermal conductivity and exhibits a larger strain and notably more misfit dislocations at the precipitate/PbTe interfaces than the other two compositions. In the PbTe-Bi 2% sample, we infer some weaker phonon scattering BiTe precipitates, in addition to the abundant Bi nanostructures. In the PbTe-Pb 2% sample, we also find that pure Pb nanoparticles exhibit stronger phonon scattering than nanostructures with Te vacancies. Within the accepted error range, the theoretical calculations of the lattice thermal conductivity in the three systems are in close agreement with the experimental measurements, highlighting the important role of misfit dislocations, nanoscale particles, and associated interfacial elastic strain play in phonon scattering. We further propose that such particle-induced local elastic perturbations interfere with the phonon propagation pathway, thereby contributing to further reduction in lattice thermal conductivity, and consequently can enhance the overall thermoelectric figure of merit.

Thermoelectric materials hold promise in devices such as power generators, heat pumps, coolers, and thermal sensors wherein they can convert thermal energy to electrical energy without any moving parts; they are reliable, lightweight, robust, and environmentally friendly.[1−3] The key issue in thermoelectrics research is to develop materials with a significantly increased thermoelectric figure of merit, $ZT = \sigma S^2 T/\kappa$, where $\sigma$ is the electrical conductivity, $S$ is the Seebeck coefficient, and $\kappa = \kappa_e + \kappa_l$ is the thermal conductivity, composed of the electronic and lattice contributions to thermal conductivity. Thus, thermoelectric performance can be improved by lowering their lattice thermal conductivity and enhancing the power factor ($\sigma S^2$).[4−7]

Modern design principles as well as synthesis and characterization approaches are bringing thermoelectric research into a new era.[8−11] Recently, materials with embedded nanoscale precipitates in bulk materials seem to show strongly reduced thermal conductivity.[12−21] Such results have raised keen interest

† Department of Materials Science and Engineering, Northwestern University.
‡ Department of Chemistry, Northwestern University.
§ Xiamen University.
|| University of Illinois at Urbana−Champaign.
⊥ Brookhaven National Laboratory.
# Argonne National Laboratory.

(1) Nolas, G. S.; Poon, J.; Kanatzidis, M. *MRS Bull.* **2006**, *31*, 199. (b) Bell, L. E. *Science* **2008**, *321*, 1457.
(2) Rowe, D. M. *CRC Handbook of Thermoelectrics*; CRC Press: New York, 1995.
(3) Rowe, D. M. *CRC Handbook of Thermoelectrics: Macro to Nano*; CRC Press: New York, 2005.
(4) Snyder, J. G.; Toberer, E. S. *Nat. Mater.* **2008**, *7*, 105.
(5) Chung, D. Y.; Hogan, T.; Brazis, P.; Rocci-Lane, M.; Kannewurf, C.; Bastea, M.; Uher, C.; Kanatzidis, M. G. *Science* **2000**, *287*, 1024.
(6) Han, M.-K.; Hoang, K.; Kong, H.; Pcionek, R.; Uher, C.; Paraskevopoulos, K. M.; Mahanti, S. D.; Kanatzidis, M. G. *Chem. Mater.* **2008**, *20*, 3512.
(7) Sootsman, J. R.; Pcionek, R. J.; Kong, H.; Uher, C.; Kanatzidis, M. G. *Chem. Mater.* **2006**, *18*, 4993.
(8) (a) Kanatzidis, M. G. *Chem. Mater.* **2010**, *22*, 648. (b) Sootsman, J. R.; Chung, D. Y.; Kanatzidis, M. G. *Angew. Chem.* **2009**, *48*, 8616. (c) Kanatzidis, M. G. In *Recent Trends in Thermoelectric Materials Research I*; Tritt, T. M., Ed.; Semiconductors and semimetals, Vol. 69; Academic Press: San Diego, 2001; p 51.
(9) Hicks, L. D.; Harman, T. C.; Sun, X. S.; Dresselhaus, M. S. *Phys. Rev. B: Condens. Matter. Mater. Phys.* **1996**, *53*, R10493.
(10) Dresselhaus, M. S.; Chen, G.; Tang, M. Y.; Yang, R.; Lee, H.; Wang, D.; Ren, Z.; Fleurial, J.-P.; Gogna, P. *Adv. Mater.* **2007**, *19*, 1043.
(11) Hochbaum, A. I.; Chen, R.; Delgado, R. D.; Liang, W.; Gamett, E. C.; Najarian, M.; Majumdar, A.; Yang, P. *Nature* **2008**, *451*, 163.
(12) Harman, T. C.; Taylor, P. J.; Walsh, P. M.; LaForge, B. E. *Science* **2002**, *297*, 2229.
(13) Venkatasubramanian, R.; Siivola, E.; Colpitts, T.; O'Quinn, B. *Nature* **2001**, *413*, 597.
(14) Hochbaum, A. I.; Chen, R.; Delgado, R. D.; Liang, W.; Garnett, E. C.; Najarian, M.; Majumdar, A.; Yang, P. *Nature* **2008**, *451*, 163.

  

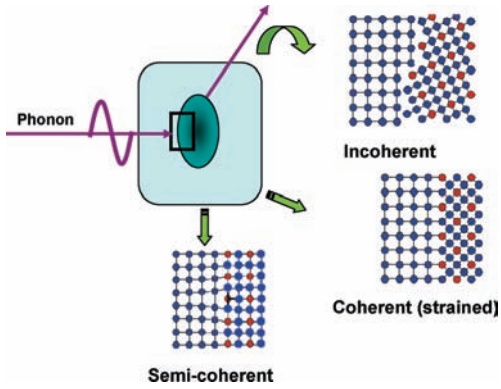


***Figure 1.*** Schematic of phonons scattered by three possible types of boundaries between matrix and nanoparticles.

in understanding nanostructuring effects. Research indicates that the low-to-mid frequency (mid-to-long wavelengths) phonons can be significantly scattered by nanostructures and the high-frequency (short wavelengths) phonons are scattered mainly by the point defects, such as solid solution alloy substitution and atom vacancies. However, the role of interfaces and associated elastic strain is unclear in relation to its influence on phonon scattering.

Figure 1 shows a schematic representation of three types of precipitate−matrix interfaces: coherent (with possible elastic strain), incoherent (with minimal interactions between the phases), and semicoherent (misfit dislocations separated by elastic strain). These three scenarios embody different atomic configurations and associated local interfacial relaxation mechanisms. We propose that not all precipitate−matrix interfaces are the same and the nature of such precipitate−matrix interfaces will have notable influence on phonon scattering at and across such interfaces. Thus, over and above the control of the size and morphology of nanoscale particles, control of interfacial characteristics is likely to be important in developing thermoelectric materials with a higher ZT.[22]

Recent reports have shown that $Ag_{1-x}Pb_mSb_yTe_{m+2}$[16] and PbTe-PbS[18] materials can achieve record-high ZT values for an n-type bulk thermoelectric, suggesting that nanostructured PbTe-based materials may offer performances better than many other materials systems. Although the emerging realization that the increased ZT of these materials is derived mainly from lower lattice thermal conductivity caused by embedded nanostructures, a complete understanding of the relations between the nanostructures and lattice thermal conductivity, especially the role of different elements in the precipitate phase and associated nature of interfaces, has remained elusive.

In this contribution, we have investigated a set of model nanostructured PbTe-based thermoelectric materials with high-resolution transmission electron microscopy (HRTEM) coupled with calculations of the lattice thermal conductivity to shed light on the fundamental issue of the relationship between nanostructures and lattice thermal conductivity. We show that among these three compositions, PbTe-2% Sb has the highest nanoparticle density, exhibits larger strain and notably more misfit dislocations at the precipitate/PbTe interfaces than the other two compositions, and therefore has the lowest measured and calculated lattice thermal conductivity. Our findings have useful implications for the understanding and optimal designing of thermoelectric materials for further improvement in their performance.

Stock PbTe was prepared from high-purity Pb (Rotometals 99.99%) and Te (Plasmaterials, 99.999%) in several 100−200 g batches in evacuated quartz ampules at 1273 K.[7] The addition of excess Pb, Bi, and Sb in the appropriate molar ratios was then carried out on a 10 g scale using Pb, Bi, and Sb metals (Tellurex, 99.999%). The samples were heated to the melt, held for 10−15 h, and then rapidly cooled from 1273 K in a room temperature water bath. The samples were examined with powder X-ray diffraction and scanning electron microscopy along with measurements of their electrical and thermal transport properties.[7] Electrical conductivity was measured using an ULVAC ZEM-3 variable temperature electrical conductivity and Seebeck coefficient system. Thermal diffusivity was measured using a Netzsch LFA 457, and the heat capacity of samples was calculated relative to a pyroceram 9606 reference. Total thermal conductivity was measured using the relation $\kappa_{tot} = \alpha C_p \delta$, where $\alpha$ is thermal diffusivity, $C_p$ is specific heat, and $\delta$ is the density of the sample, calculated from sample dimensions and mass. Lattice thermal conductivity was calculated using the Wiedemann−Franz relation assuming an $L_0$ of $2.45 \times 10^{-8}$ $W\Omega K^{-2}$. The thin sections of the specimens were examined under scanning transmission or transmission electron microscopy (S/TEM) mode with JEOL 2100F, 3000F, and 2200FS with spherical aberration (Cs) corrector transmission electron microscopes. TEM samples were prepared by conventional methods, with due care to mechanical and ion beam damage. The samples were cut into 3-mm-diameter discs by a disk cutter, then ground, dimpled, polished, and subsequently Ar-ion milled on a stage cooled with liquid nitrogen. High-resolution images were simulated with the MacTempas program code[23] with the following parameters as input: spherical aberration of 1 mm, defocus spread of 8 nm, semiconvergence angle of illumination of 0.55 mrad, and a 7 $nm^{-1}$ diameter of the objective lens' aperture.

TEM investigation of the three samples of PbTe-2% X (X = Sb, Bi, or Pb) shows nanoscale precipitates with a lower nanoparticle density in PbTe-Bi 2% and PbTe-Pb 2% samples and with a higher nanoparticle density in the PbTe-Sb 2% sample. Most precipitates in all samples have a regular spherical-like shape, except for PbTe-Pb 2% in which we also observed some very narrow platelet-like precipitates. Figure 2 shows typical low magnification images of the samples with a different nanoparticle density. In Figure 2a lower densities of both weak contrast spherical- and platelet-like nanoscale precipitates were

(15) Boukai, A.; Bunimovich, Y.; Tahir-Kheli, J.; Yu, J.-K.; Goddard, W. A., III; Heath, J. R. *Nature* **2008**, *451*, 168.
(16) Hsu, K. F.; Loo, S.; Guo, F.; Chen, W.; Dyck, J. S.; Uher, C.; Hogan, T.; Polychroniadis, E. K.; Kanatzidis, M. G. *Science* **2004**, *303*, 818.
(17) Poudeu, P. F.; D'Angelo, J.; Kong, H.; Downey, A.; Short, J. L.; Pcionek, R.; Hogen, T. P.; Uher, C.; Kanatzidis, M. G. *J. Am. Chem. Soc.* **2006**, *128*, 14347.
(18) Androulakis, J.; Lin, C.-H.; Kong, H.-J.; Uher, C.; Wu, C.-I.; Hogan, P. T.; Cook, B. A.; Calliet, T.; Paraskevopoulos, K. M.; Kanatzidis, M. G. *J. Am. Chem. Soc.* **2007**, *129*, 9780.
(19) Sootsman, J.; Kong, H.; Uher, C.; D'Angelo, J.; Wu, C.-I.; Hogan, T. P.; Caillat, T.; Kanatzidis, M. G. *Angew. Chem., Int. Ed.* **2008**, *47*, 8618.
(20) Poudel, B.; Hao, Q.; Ma, Y.; Lan, Y.; Minnich, A.; Yu, B.; Yan, X.; Wang, D.; Muto, A.; Vashaee, D.; Chen, X.; Liu, J.; Dresselhaus, M. S.; Chen, G.; Ren, Z. *Science* **2008**, *320*, 634.
(21) Zhou, M.; Li, J.-F.; Kita, T. *J. Am. Chem. Soc.* **2008**, *130*, 4527.
(22) Androulakis, J.; Hsu, K. F.; Pcionek, R.; Kong, H.; Uher, C.; Dangelo, J.; Downey, A. D.; Hogen, T. P.; Kanatzidis, M. G. *Adv. Mater.* **2006**, *18*, 1170.
(23) HRTEM Image Simulation Software Package. http://www.totalresolution.com/.

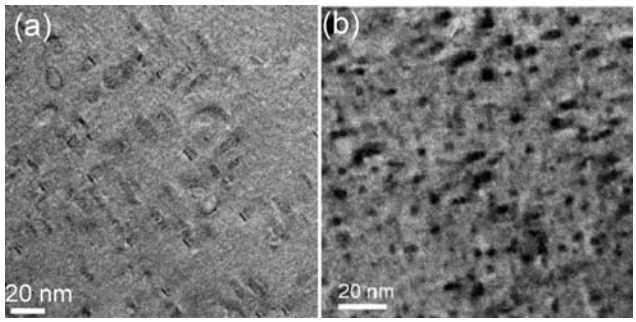


***Figure 2.*** Typical images of two samples: PbTe-Pb 2% (a) and PbTe-Sb 2% (b). (a) The image shows two types of nanoscale precipitates: one is a regular spherical-like shape; another one is a platelet-like shape. (b) The image has only one regular type of precipitate. From comparison of the two images, (b) has a higher nanoscale precipitate density than (a).

observed in the PbTe-Pb 2% sample similar to those reported in ref 24. The spherical-like precipitates show a 2-fold increase in density distribution with respect to the platelet-like precipitates. In Figure 2b, the image of the sample PbTe-Sb 2% depicts higher density nanoscale precipitates with a dark contrast and a size distribution of 1−10 nm. Although it is difficult to quantitatively determine the compositions of precipitates due to overlap with the matrix, we have observed a higher intensity of Sb and Bi in the precipitates (dark areas) by energy dispersion X-ray spectroscopy (EDS) for samples PbTe-Sb 2% and PbTe-Bi 2%, respectively.

To analyze the strain distribution at the boundaries between the nanoinclusions and the PbTe matrix, we have examined PbTe-Pb 2% (Figure 3), PbTe-Bi 2% (Figure 4), and PbTe-Sb 2% (Figure 5) interfaces at the atomic level with HRTEM. Figure 3a is the lattice image of one precipitate in sample PbTe-Pb 2% along the $[001]_{PbTe}$ direction. This precipitate has a lattice parameter very close to that of the matrix PbTe. Figure 3b is a representative high resolution TEM image of a platelet-like precipitate, obtained with the electron beam parallel to the $[010]_{PbTe}$ axis. Examining the contrast of the defect feature in Figure 3a and b, reminiscent of vacancy coalescence, we believe that the precipitates are likely comprised of Te vacancies within the PbTe region. Figure 3c shows a model of a Te deficient PbTe precipitate in the nominally stoichiometric PbTe matrix. The simulated image based on this model when inserted into Figure 3b agrees well with the experimental result within the constraints of experimental parameters. Although the platelet-like precipitates are mainly dominated by Te vacancies, we have also observed platelet-like precipitates, inferred to be rich in Pb. Figure 3d is the STEM image of one platelet-like precipitate. Figure 3e is the enlarged image in a boxed area of Figure 3d. The platelet-like Pb precipitate links the antiphase domains of PbTe separated by a pair of partial dislocations with a Burger vector of 1/2 [100]. Figure 3f is the atomic level model, which illustrates the likely atomic structure of the Pb (rich) precipitate.

In a representative Figure 4a, the PbTe-Bi 2% sample shows precipitates of a 2−4 nm size distribution in this image, although the range of sizes spans ∼1−10 nm in the entire sample. Most of the precipitates are detected as Bi, while a few precipitates, for example in Figure 4b which is an enlarged part from Figure 4a, clearly show different structures from Bi precipitates. Two types of antiphase boundaries are seen in/around this precipitate: a conservative antiphase boundary (APB) (horizontal red

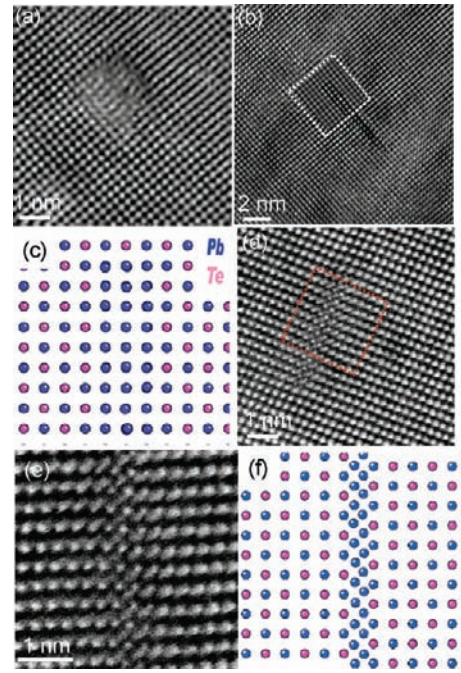


***Figure 3.*** (a) High magnification atomic resolution lattice image along [001] direction of one typical precipitate in sample PbTe-Pb 2% reveals the precipitate has similar structure and the same lattice parameter as those of the PbTe matrix. (b) Lattice image along [010] direction shows the dark line precipitate has a short *c* direction. (c) is the structure modeling, where blue dots are Pb atomic columns and purple dots are Te atomic columns, the simulated image according to the model inset in (b). (d) The STEM image depicts another type of platelet-like nanoscale precipitate. Its enlarged part image is shown in (e), and (f) is the structure model of the precipitate and matrix.

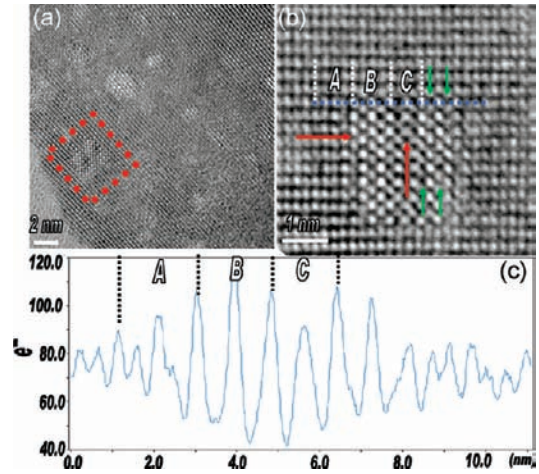


***Figure 4.*** (a) High resolution TEM image of sample PbTe-Bi 2% shows some precipitates with size distribution of 1−4 nm. (b) is the enlarged image boxed in (a), which reveals that the precipitate has a different structure from the matrix and conservative antiphase boundary. (c) Line scanning profile blue line in (b) shows $B = 8.87$ Å, $C = 7.8$ Å, with *A* selected as standard calibration.

arrowhead) with a 1/2 unit cell shift (marked by green arrowheads) and a nonconservative antiphase boundary (perpendicular red arrowhead) depicting one missing lattice plane, similar to the observations in ref 25. A line scan profile across this nonconservative APB (blue line in Figure 4b is shown in

(24) Ke, X. Z.; Chen, C. F.; Yang, J. H.; Wu, L. J.; Zhou, J.; Li, Q.; Zhu, Y. M.; Kent, P. R. C. *Phys. Rev. Lett.* **2009**, *103*, 145502.

(25) He, J. Q.; Vasco, E.; Dittmann, R.; Wang, R. H. *Phys. Rev. B* **2005**, *73*, 125413.

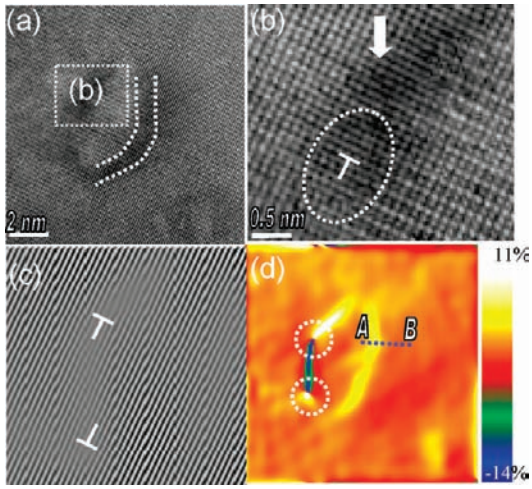


***Figure 5.*** (a) High-magnification lattice image of PbTe-Sb 2% depicts clearly the boundary between precipitate and matrix. (b) Enlarged image of box in (a) shows a misfit dislocation at the precipitate/matrix boundary. (c) IFFT image shows two dislocation cores in this precipitates. (d) The strain distribution of the nanoscale inclusions clearly show the two dislocation cores on the right side and a highly strained boundary on the left side.

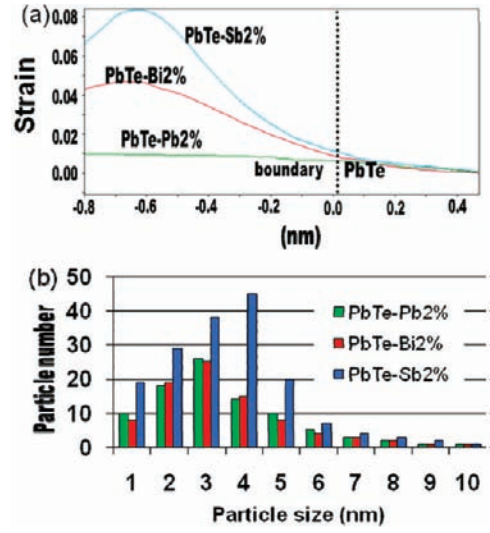


***Figure 6.*** (a) Average strain distributions of boundaries between nanoscale inclusions and matrixes in PbTe-Sb 2% (blue curve), PbTe-Bi 2% (red curve), and PbTe-Pb 2% (green curve). (b) Under the same volume, histograms of nanoscale precipitates in PbTe-Pb 2% (green), PbTe-Bi 2% (red), and PbTe-Sb 2% (blue).

Figure 4c). If we use the lattice parameter of PbTe (marked *A* in Figure 4b and c) as a reference, the *B* and *C* distances are 0.88 and 0.78 nm, respectively. The lattice parameters of this precipitate are determined to be close to those of PbTe, which exactly do not correspond to that of elemental Bi, but rather a likely BiTe phase which is also cubic with a lattice parameter of 0.647 nm. The new BiTe precipitates originate from a chemical reaction between the PbTe matrix and Bi. A possible reaction can be expressed as follows:

$$\mathrm{Bi} + \mathrm{PbTe} \rightarrow \mathrm{BiTe} + \mathrm{Pb} \qquad (1)$$

With $\Delta G^{\circ}_{1300\mathrm{K}} = -62.89$ kJ/mol.[26] Although this reaction may not be the most favorable, its existence indicates that the PbTe/Bi boundary is thermodynamically metastable at 1300 K.

Figure 5a is the HRTEM image of a 4 nm precipitate in the PbTe-Sb 2% sample. One interfacial boundary (~1 nm dark contrast) between the matrix and precipitate is observed. Figure 5b is the enlarged lattice image of the boxed area, which clearly shows a dislocation at the boundary marked by an oval dotted line. In Figure 5c the inverse fast Fourier transform (IFFT) image of the precipitate depicts two dislocation cores at the boundary. Burger's circuit around the dislocation core in Figure 5b yields a closure failure with a projected vector of 1/2 a[010]. A high strain region is found at the boundary region pointed out by a vertical arrowhead. To analyze the strain in detail, this image was studied by geometric phase analysis (GPA),[27,28] which is a lattice image processing method for strain field analysis. GPA was used to investigate the variation in the lattice parameter, thus the elastic strain at/around the boundaries. To reduce the artifacts of the strain analysis, it is necessary to obtain and use high quality, clear lattice images. Figure 5d is the strain map profile along the 001 direction ($\varepsilon_{yy}$) showing two highly strained dislocation cores, with yellow indicating expansion and blue compression (see the color scale). From the strain map distribution of this image, it is clear the arrowhead-indicated precipitate/matrix boundary is highly strained.

From such detailed TEM observations, it is obvious that all three compositions have variable strain at the precipitate/matrix boundaries. After the processing and analysis of more than 10 precipitates, the largest strained boundaries were found in the sample PbTe-Sb 2% while the smallest strained boundaries were found in the PbTe-Pb 2% specimens. Figure 6a shows typical line scan profiles of the boundaries between the matrix and precipitate for all three samples at 300 K. The misfit of boundaries in sample PbTe-Sb 2% (blue curve) is ~8% while for sample PbTe-Bi 2% (red curve) it is ~4%; however for sample PbTe-Pb 2% (green curve) it is only 1% or less.

Figure 6b shows the size distribution for all three samples under the same TEM observation volume. It is clear that the PbTe-Sb 2% sample has the highest density of precipitates, approximately two times more than the PbTe-Pb 2% or PbTe-Bi 2%. However, all samples have an average particle size of 2−4 nm. On average, the estimates of the distribution density and size of all types of nanoscale precipitates are as follows: ~$1 \times 10^{12}$/cm$^2$, ~4 nm for PbTe-Sb 2%; (2−4) × $10^{11}$/cm$^2$, 2−3 nm for PbTe-Pb 2% and PbTe-Bi 2% samples. We note that although the size distributions of the precipitates are relatively broad (range of 1−10 nm), the strains at the boundaries of precipitates with different sizes are still quite similar. We also note that many misfit dislocations appear in almost every precipitate observed at the precipitate/matrix boundary in sample PbTe-Sb 2%, which means that the density of dislocations is similar to that of precipitates while only a few dislocations are observed in the PbTe-Bi 2% and PbTe-Pb 2% specimens.

Overall, the observed nanoscale architecture comprising the precipitates, interfacial region, and associated local strain are all likely to enhance phonon scattering and thus reduce the lattice thermal conductivity in these systems. To evaluate the phonon scattering mechanisms of the precipitates in the PbTe-based materials in more detail, we performed theoretical calculations

(26) Knacke, O.; Kubaschewski, O.; Hesselmann, K. *Thermochemical properties of inorganic substances*; Springer: Berlin, 1991.
(27) Hytch, M. J.; Snoeck, E.; Kilaas, R. *Ultramicroscopy* **1998**, *74*, 131.
(28) He, J. Q.; Gueguen, A.; Sootsman, J.; Zheng, J. C.; Wu, L.; Zhu, Y.; Kanatzidis, M. G.; Dravid, V. P. *J. Am. Chem. Soc.* **2009**, *131*, 17828.

of the lattice thermal conductivity using a theory of relaxation time of phonons based on the Debye model,[29]

$$\kappa_{\mathrm{lat}} = \frac{k_{\mathrm{B}}}{2\pi^2 v}\left(\frac{k_{\mathrm{B}}T}{\hbar}\right)^3 \left\{ \int_0^{\theta_{\mathrm{D}}/T} \tau_{\mathrm{c}} \frac{x^4 e^x}{(e^x-1)^2}\mathrm{d}x + \frac{\left[\int_0^{\theta_{\mathrm{D}}/T} \frac{\tau_{\mathrm{c}}}{\tau_{\mathrm{N}}} \frac{x^4 e^x}{(e^x-1)^2}\mathrm{d}x\right]^2}{\int_0^{\theta_{\mathrm{D}}/T} \frac{1}{\tau_{\mathrm{N}}}\left(1-\frac{\tau_{\mathrm{c}}}{\tau_{\mathrm{N}}}\right)\frac{x^4 e^x}{(e^x-1)^2}\mathrm{d}x} \right\} \quad (2)$$

where $k_{\mathrm{B}}$ is the Boltzmann's constant, $\hbar$ is the Plank constant, $T$ and $\theta_{\mathrm{D}}$ are respectively the absolute temperature and Debye temperature, $v$ is an average phonon-group velocity, $x = \hbar\omega/k_{\mathrm{B}}T$, $\tau_N$ is the relaxation time due to normal phonon−phonon scattering, and $\tau_{\mathrm{c}}$ is the combined relaxation time. The latter is obtained by integrating the relaxation times from various processes. From our TEM studies, at a certain frequency, the relaxation time mainly is primarily related to scattering from the strain, nanoscale precipitates, dislocations, boundaries, and the phonon−phonon interactions:

$$\tau_{\mathrm{c}}^{-1} = \tau_{\mathrm{U}}^{-1} + \tau_{\mathrm{N}}^{-1} + \tau_{\mathrm{B}}^{-1} + \tau_{\mathrm{D}}^{-1} + \tau_{\mathrm{P}}^{-1} + \tau_{\mathrm{S}}^{-1} \quad (3)$$

where $\tau_{\mathrm{U}}$, $\tau_{\mathrm{N}}$, $\tau_{\mathrm{B}}$, $\tau_{\mathrm{D}}$, $\tau_{\mathrm{P}}$, and $\tau_{\mathrm{S}}$ are the relaxation times corresponding to scattering from Umklapp processes, normal processes, boundaries, dislocations, precipitates, and strains respectively. The first five mechanisms have been investigated previously.[30−37]

The last variable, $\tau_{\mathrm{S}}$, is due to scattering from the localized and distributed strain in the vicinity of the precipitates and associated interfaces, which has seldom received attention due to the difficulties of accurately measuring the elastic strain. To understand the effect of the strain field on lattice thermal conductivity, we have performed first principles calculations based on linear response density functional theory (DFT)[38] to investigate the phonon properties of PbTe under various strain conditions. The DFT calculations show that, under tensile hydrostatic strain, phonon modes are softened and the stiffness of PbTe decreases. The speed of sound in PbTe is reduced accordingly, since it is proportional to the square-root of stiffness, which is very sensitive to strain.[39,40] For in-plane tensile or compressive strains, the low-frequency phonons are softened while high-frequency phonons are stiffer. The thermal conductivity is a result of the competition between the strain-induced modification of low-frequency and high-frequency phonons. However, it is mainly dominated by the variation of low-frequency phonons, and thus the lattice thermal conductivity reduces to a smaller value. For example, for 2% in-plane tensile strain, as shown in Figure 7, the acoustic phonon frequency decreases ~20%. Due to high temperatures, e.g., 300−700 K, studied in this work, the Umklapp processes are important in scattering heat-conducting phonons.[41] We estimate the strain-induced reduction of the lattice thermal conductivity based on a model[42,43] that can be used to calculate lattice thermal conductivity from phonon spectra and has been shown to be applicable to a wide range of crystal structures and compounds. According to this model, the thermal conductivity largely depends on the Debye temperature of acoustic phonons, which can be written as $\Theta_{a,i} = (\hbar\omega_{a,i})/(k_{\mathrm{B}})$ for each acoustic phonon branch $i$. If we assume the acoustic phonon mode Grüneisen parameter is invariant for small strains, then the thermal conductivity can be expressed as $\kappa \propto \Theta_{a,i}^3$, and the reduction of thermal conductivity can be as large as 50% for 2% in-plane tensile strain. Our DFT calculations clearly indicate that strain field can play an important role on reducing thermal conductivity at high temperature. This provides a more fundamental basis for our further analysis of strain effects based on Debye's model, as we will present in great detail below.

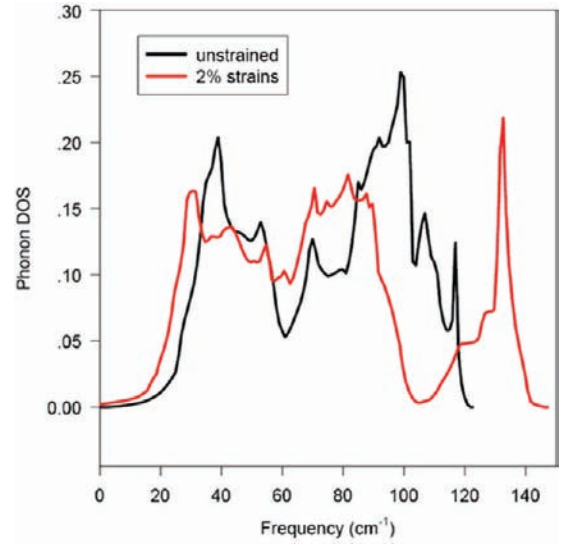


***Figure 7.*** Phonon density of states (DOS) versus the phonon frequency under 2% in-plane tensile strain of PbTe determined by DFT calculation. The low-frequency DOS part is mainly contributed by acoustic modes, and the high-frequency part is from optical modes. The acoustic phonon frequency decreases ~20% for 2% strain compared with the unstrained one, as clearly shown by the shift of the first peak. This will lead to a significant reduction of the lattice thermal conductivity, as discussed in the text.

To simplfy our calculation, the relaxation time due to elastic strain field, $\tau_{\mathrm{S}}$, is given by Peter Carruthers[44]

$$\tau_{\mathrm{s}}^{-1} = \frac{1}{4}\sigma\left(\frac{gA'}{\rho}\right)^2\left(\frac{q^2}{v^3}\right) = \frac{144\sigma\gamma^2\varepsilon^2 r_0^4}{v}\omega^2 \quad (4)$$

where $g = 24\gamma\rho v^2$, $A' = \varepsilon r_0^2$, $q = (\omega)/(v)$, $\rho$ is the density of the crystal, $\sigma$ is the scatter density, $r_0$ is the radius of the sphere,

(29) Callaway, J.; Von Baeyer, H. C. *Phys. Rev.* **1960**, *120*, 1149.
(30) Morelli, D. T.; Heremans, J. P. *Phys. Rev. B* **2002**, *66*, 195304.
(31) He, J. Q.; Girard, S. N.; Kanatzidis, M. G.; Dravid, V. P. *Adv. Funct. Mater.* **2010**, *20*, 764.
(32) Chen, G.; Dames, C.; Song, D.; Harris, C. T. *Thermal conductivity 27/thermal expansion 15*; Huang, H., Porter, W., Eds.; DEStech Publications: Lancaster, PA, 2004; p 263.
(33) Chen, G.; Zeng, T.; Borca-Tascius Song, T. D. *Mater. Sci. Eng.* **2000**, *292*, 155.
(34) Zou, J.; KotchetKov, D.; Balandin, A. A.; Florescu, D. I.; Pollak, F. H. *J. Appl. Phys.* **2002**, *92*, 2534.
(35) Kim, W.; Singer, S. L.; Majumdar, A.; Zide, J. M. O.; Klenov, D.; Gossard, A. C.; Stermer, S. *Nano Lett.* **2008**, *8*, 2097.
(36) Kim, W.; Majumdar, A. *J. Appl. Phys.* **2006**, *99*, 084306.
(37) Mingo, N.; Hauser, D.; Kobayashi, N. P.; Plissonnier, M.; Shakouri, A. *Nano Lett.* **2009**, *9*, 711.
(38) Giannozzi, P.; et al. *J. Phys.: Condens. Matter* **2009**, *21*, 395502.
(39) Picu, R. C.; Borca-Tasciuc, T.; Pavel, M. C. *J. Appl. Phys.* **2003**, *93*, 3535.
(40) Bhowmick, S.; Shenoy, V. B. *J. Chem. Phys.* **2006**, *125*, 164513.
(41) Zhang, Y; Ke, X. Z.; Chen, C.; Yang, J.; Kent, P. R. C. *Phys. Rev. B* **2009**, *80*, 024304.
(42) Slack, G. A. *Solid State Phys.* **1979**, *34*, 1.
(43) Morelli, D. T.; Heremans, J. P. *Appl. Phys. Lett.* **2002**, *81*, 5126.
(44) Carruthers, P. *Rev. Mod. Phys.* **1961**, *33*, 92.

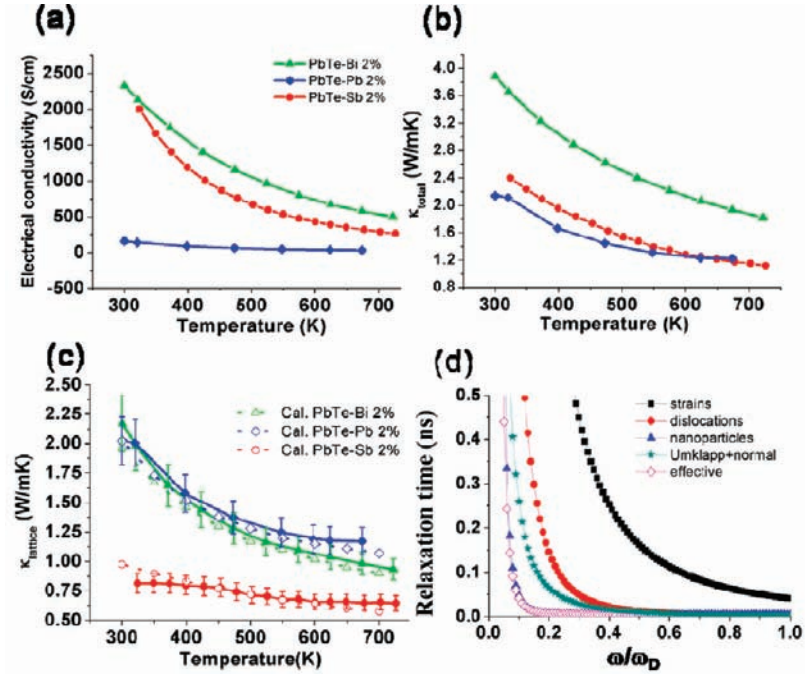


***Figure 8.*** Temperature dependence of electrical conductivity (a), total thermal conductivity (b), and lattice thermal conductivity (c) of PbTe-Pb2%, PbTe-Bi 2%, and PbTe-Sb 2% (diamonds, triangles, and circles, respectively). In (c) the open diamonds, triangles, and squares are the theoretical calculations based on TEM observations. (d) Relaxation time versus the normalized frequency of PbTe-Sb 2% at 300 K. The phonon frequency ($\omega$) is normalized to the Debye frequency ($\omega_D$).

and $\varepsilon$ is the misfit between the sphere and the matrix. The misfit has a dependence on temperature, which can be written as

$$\varepsilon = \varepsilon_0 + [\alpha_P - \alpha_M(1 - \varepsilon_0)](T - 300) \qquad (5)$$

where $\varepsilon_0$ is the misfit at room temperature (300 K) which can be obtained from Figure 6a, and $\alpha_P$ and $\alpha_M$ are the thermal expansion coefficients of the precipitate and matrix, respectively. The coefficients of thermal expansion of Pb, Bi, Sb, and PbTe are $29.1 \times 10^{-6}$/K, $13.4 \times 10^{-6}$/K, $8.5 \times 10^{-6}$/K, and $19.8 \times 10^{-6}$/K, respectively.

Based on these formulas and the parameters obtained from TEM observations and ref 31, we have calculated the lattice thermal conductivity of nanostructured-PbTe-Pb 2%, PbTe-Bi 2%, and PbTe-Sb 2%.[45] For comparison, here we also include measured electrical transport properties of all three samples: PbTe-X (X = 2% Sb, Bi, or Pb). In Figure 8a, the electrical conductivity of PbTe-Sb 2% is quite similar to that of PbTe-Bi 2%; this indicates electron scattering is not proportional to the strain strength and dislocation density. However, the electrical conductivity of PbTe-Pb 2% is much lower than those of the other two, which suggests the platelet-like precipitates have very strong electron scattering and reduce electron mobilities. The total thermal conductivity (Figure 8b) of the PbTe-Bi 2% sample is 4 W/mK at room temperature and 1.7 W/mK at 700 K, which is almost twice those of the other two samples. Figure 8c shows the plots of the experimental and calculated lattice thermal conductivity of the three samples, the error bars in the measured data mainly resulting from instrumental errors. Within the margin of error, the agreement between calculated and experimental data for the three samples reinforces the validity of the argument that dislocations, strains, and nanoscale precipitates all significantly reduce the lattice thermal conductivity. Our calculations further suggest that Pb nanocrystals have stronger phonon scattering than Te vacancy PbTe in the PbTe-Pb 2% sample, and likewise Bi particles have a stronger phonon scattering than BiTe precipitates in PbTe-Bi 2% sample.

For the sample PbTe-Sb 2%, the plots of relaxation times based on theoretical data on some of the above possible contributing terms are shown in Figure 8d. Collectively, it suggests that dislocations cause strong, high-frequency phonon (>0.6 $\omega_D$) scattering, and nanoscale particles appear to dominate phonon scattering with frequencies below 0.6 $\omega_D$. Strain at the boundaries also induces strong, low-frequency phonon (<0.15 $\omega_D$) scattering; however it is weaker than nanoparticles. Though somewhat intuitively obvious, this contribution provides a comprehensive account reflecting the consistency between experimental observations and theoretical calculations of the nanoparticle induced phonon scattering in PbTe-based thermoelectric materials and thus explains their greatly reduced (lattice) thermal conductivity.

## Conclusions

Advanced TEM can delineate the detailed nanostructure of Sb, Bi, and Pb embedded in PbTe thermoelectric materials and shed new light regarding their influence on the thermoelectric figure of merit, more specifically on its lattice thermal conductivity. The study reveals that dislocations, nanoscale particles/precipitates, and strain play an important role in increasing phonon scattering thus reducing the lattice thermal conductivity of this system. The theoretical calculations of lattice conductivity are consistent with the measured experimental values, indicating the validity of the approach and premise. This work also teaches that the mere presence of nanostructuring in the semiconductor

(45) The calculation of lattice thermal conductivity of PbTe-Pb 2% sample included the fact that sizes of lead nanoparticles will shrink at high temperature due to their high interdiffusion after melting. Note: our *in situ* TEM experiment showed some lead nanoparticles start to melt at 400 K. It also revealed that the melting temperature depends on the size of lead nanoparticles, which is in agreement with Coombes's observation (Coombes, C. J. *J. Phys. F: Met. Phys.* **1972**, *2*, 441).

is not enough to increase phonon scattering. What is required is the use of appropriate nanoprecipitates which create large mass contrast, significant strain fields (elastic strain), and dislocations (plastic and elastic strain).

**Acknowledgment.** Financial support from the Office of Naval Research is gratefully acknowledged. Transmission electron microscopy work was performed in the (EPIC) (NIFTI) (Keck-II) facility of the *NUANCE* Center at Northwestern University. The *NUANCE* Center is supported by NSF-NSEC, NSF-MRSEC, Keck Foundation, the State of Illinois, and Northwestern University. J.C.Z. is supported by the Minjiang Scholar Distinguished Professorship Program through Xiamen University of China, Specialized Research Fund for the Doctoral Program of Higher Education (Grant No. 20090121120028), and the Natural Science Foundation of Fujian Province, China (Grant No. 2009J01015). Portions of TEM work done at BNL were supported by the DOE Office of Science under Contract No. DEAC02-98CH10886.

**Supporting Information Available:** Complete ref 38. This material is available free of charge via the Internet at http://pubs.acs.org.

JA1010948